

# RSC Applied Interfaces

Accepted Manuscript

This article can be cited before page numbers have been issued, to do this please use: G. Nunziata, M. Sponchioni and F. Rossi, *RSC Appl. Interfaces*, 2026, DOI: 10.1039/D6LF00061D.



This is an Accepted Manuscript, which has been through the Royal Society of Chemistry peer review process and has been accepted for publication.

Accepted Manuscripts are published online shortly after acceptance, before technical editing, formatting and proof reading. Using this free service, authors can make their results available to the community, in citable form, before we publish the edited article. We will replace this Accepted Manuscript with the edited and formatted Advance Article as soon as it is available.

You can find more information about Accepted Manuscripts in the [Information for Authors](#).

Please note that technical editing may introduce minor changes to the text and/or graphics, which may alter content. The journal's standard [Terms & Conditions](#) and the [Ethical guidelines](#) still apply. In no event shall the Royal Society of Chemistry be held responsible for any errors or omissions in this Accepted Manuscript or any consequences arising from the use of any information it contains.

# Programmable Shrinking and Aggregation of pH- Thermo Dual-Responsive Amphiphilic Polymeric Nanoparticles Governed by Molecular Architecture

View Article Online  
DOI: 10.1039/C6AF00061D

*Giuseppe Nunziata, Mattia Sponchioni \* and Filippo Rossi \**

*Department of Chemistry, Materials and Chemical Engineering “Giulio Natta”, Politecnico di  
Milano, via Edoardo Bassini 6, 20133, Milan, Italy*

\* corresponding authors

E-mail: [mattia.sponchioni@polimi.it](mailto:mattia.sponchioni@polimi.it)

[filippo.rossi@polimi.it](mailto:filippo.rossi@polimi.it)



**ABSTRACT**View Article Online  
DOI: 10.1039/D6LF00061D

Stimuli-responsive polymeric nanoparticles represent powerful drug delivery systems capable of responding to pathological microenvironments. However, most dual-responsive platforms are treated as binary on/off systems, and a predictive framework linking molecular architecture to nanoparticle structural evolution upon application of the stimulus is still lacking. Here, we report a modular library of amphiphilic block copolymers combining a hydrophobic polylactic acid (PLA) core-forming segment, a pH-responsive polymethacrylic acid (PMAA) stabilizing block, and a thermo-responsive poly(ethylene glycol) methyl ether methacrylate (PEGMA)-based corona, enabling programmable nanoparticle behavior across physiological pH and temperature ranges. Systematic variation of block composition and length allowed independent tuning of nanoparticle size (78-244 nm), surface charge (-53 to -4 mV), phase transition temperature (30-44 °C), and critical micelle concentration (1.55-15.82 mg L<sup>-1</sup>), while preserving narrow particle size distribution and excellent colloidal stability. Importantly, the presence of PMAA segment fundamentally altered the thermo-responsive mechanism. While without PMAA the nanoparticles underwent aggregation above the phase transition temperature, with large positive size increase, PMAA-containing nanoparticles exhibited controlled and reversible intraparticle corona collapse, resulting in predictable shrinking without loss of colloidal integrity. To rationalize this behavior, we introduced a structural growth number (GN), a phenomenological descriptor capturing the balance between corona collapse, electrostatic stabilization and hydrophobic aggregation. A monotonic correlation between GN and thermo-responsive-induced size variation demonstrates that nanoparticle fate can be structurally programmed, enabling precise switching between shrinking and aggregation regimes. This modular platform establishes a predictive design strategy for dual-responsive nanocarriers and provides a foundation for engineering adaptive drug delivery systems capable of controlled size modulation and localized activation in complex biological environments.

**KEYWORDS:** colloids, drug delivery, nanoparticles, pH-responsive, thermo-responsive.



## Introduction

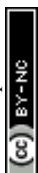
Stimuli-responsive polymeric nanoparticles have emerged as promising platforms for adaptive drug delivery, as their structural organization can dynamically respond to local changes in environment parameters such as pH and temperature <sup>1-4</sup>. Gradients of these parameters are particularly relevant in pathological tissues, including tumors and inflamed regions, where extracellular acidosis and mild hyperthermia create conditions significantly different from those found in healthy physiological environments <sup>5</sup>. The ability to translate these subtle physicochemical changes into predictable nanoscale structural transitions provides a powerful strategy to enhance targeting efficiency, control drug release and improve therapeutic selectivity <sup>6-9</sup>. From a pharmaceutical perspective, these physicochemical features are particularly relevant for pathological conditions in which local microenvironmental gradients can be exploited as endogenous activation cues. Solid tumors represent a major example, as they are frequently associated with extracellular acidosis, abnormal vascular permeability, impaired lymphatic drainage, and locally increased temperature arising from enhanced metabolic activity or externally applied mild hyperthermia <sup>10</sup>. Similar considerations apply to inflamed tissues, where immune-cell infiltration and altered metabolism can generate acidic and warmer microenvironments compared to healthy tissues <sup>11</sup>. In such scenarios, pH- and thermo-responsive nanoparticles may provide a rational basis for designing nanocarriers with improved spatial control over stability, accumulation, and release behavior <sup>12</sup>. Thermo-responsive polymeric nanoparticles have also been explored for localized and sustained delivery in volume-restricted tissues, such as the eye, as well as for advanced biomedical applications including gene delivery and imaging <sup>13</sup>. Within this broader pharmaceutical framework, the possibility to program nanoparticle shrinking or aggregation is especially attractive: shrinking systems may favor tissue penetration and cellular uptake, whereas aggregation-prone systems may support local retention and depot formation<sup>14</sup>.



These considerations highlight the relevance of establishing structure–responsivity relationships that allow nanocarrier behavior to be matched to specific pathological microenvironments. In this context, PLA-containing methacrylate macromonomers, including HEMA-graft-lactide derivatives, have previously been reported as versatile building blocks for the preparation of degradable polymer architectures<sup>15</sup>. Their combination with controlled radical polymerization strategies offers a convenient route to amphiphilic polymer systems in which hydrophobic, degradable domains can be integrated with functional responsive segments. Thermo-responsive polymers typically rely on a temperature-dependent balance between polymer-polymer and polymer-water interactions, leading to a reversible phase transition at a characteristic critical temperature<sup>16,17</sup>. Polymers exhibiting a lower critical solution temperature (LCST) are soluble and highly hydrated below this threshold, while undergoing dehydration and collapse upon heating<sup>18,19</sup>. Poly(N-isopropylacrylamide) (PNIPAM) has historically been the most widely investigated thermo-responsive polymer, due to its LCST (*i.e.* 32 °C) close to physiological temperature<sup>20</sup>. However, alternative systems based on oligo(ethylene glycol) methacrylates (EGMAs), could offer several key advantages. EGMA-based polymers display excellent biocompatibility and bio-inertness, reduced protein adsorption, and highly reversible thermal transitions with minimal hysteresis<sup>21,22</sup>. Their phase separation temperature (PST) can be finely tuned through macromolecular design by adjusting the lengths of the polymer backbone and of the oligo(ethylene glycol) side chains, as well as by copolymerization<sup>23</sup>. This compositional versatility makes EGMA-based polymers a particularly attractive platform for engineering thermo-responsive nanostructures<sup>24</sup>. In nanoparticle systems, thermo-responsivity is not only driven by the intrinsic properties of the responsive block, but also by its architectural context<sup>25</sup>. The confinement of thermo-responsive chains at the core-shell interface, their degree of stretching and hydration, and the nature of the underlying core can strongly influence both the transition temperature and the outcomes of this transition<sup>26</sup>.



Indeed, thermo-induced responses can range from subtle, intraparticle reorganizations to aggregation-dominated transitions, depending on the balance between attractive and stabilizing interactions within the assembly<sup>27,28</sup>. pH-responsive polymers, on the other hand, exploit a complementary mechanism, based on the ionization of acidic or basic functional groups<sup>29,30</sup>. Methacrylic acid (MAA) is among the most employed monomers for this purpose, as protonation of its carboxylic groups at acidic pH leads to a pronounced reduction of electrostatic repulsion and hydration, promoting chain association and structural rearrangement<sup>31</sup>. In polymeric nanoparticles, the extent and sharpness of the pH-responsive transition are governed not only by the presence of MAA, but also by its effective density, spatial distribution, and interaction with other blocks in the architecture<sup>32</sup>. Variations in MAA content have been shown to directly affect surface charge, colloidal stability, and the pH threshold at which size changes and aggregation phenomena are observed, as typically captured by dynamic light scattering (DLS) and zeta-potential measurements<sup>33</sup>. In this context, combining pH- and thermo-responsiveness within a single nanocarrier represents an attractive strategy to further refine control over nanoparticle stability and drug release<sup>34</sup>. Dual-responsive systems can exploit the coexistence of multiple physicochemical gradients in pathological tissues, where mild acidosis often occurs together with local temperature variations associated with inflammation or high metabolic activity<sup>35</sup>. While several examples of pH/thermo-responsive core-shell nanoparticles have been reported, these systems are often treated as binary “on/off” platforms, where responsiveness is demonstrated but not systematically tuned<sup>36</sup>. In particular, the interplay between polymer composition, block architecture and nanoparticle core characteristics is rarely explored as a design parameter to modulate the amplitude, direction, and mechanism of the thermally induced size transition or the pH-triggered structural rearrangement<sup>37</sup>. As a result, a comprehensive structure-responsivity relationship for dual-responsive nanoparticles is still lacking.



In this work, we address this challenge by investigating a well-defined library of dual pH- and thermo-responsive block copolymers designed to self-assemble into nanoparticles with programmable behavior. More specifically, we combined 2-hydroxyethyl methacrylate (HEMA) grafted with PLA chains with MAA in a statistic copolymer, which was then chain-extended with a poly(EGMA) segment to form amphiphilic macromolecules. These were demonstrated to self-assemble in aqueous environments into core-shell nanoparticles, with a core expectedly formed by the PLA pendant chains, the pH-responsive MAA units exposed to water and the thermo-responsive EGMA segment in the corona. By systematically varying the degree of polymerization and relative block composition, we established a modular platform in which both pH- and temperature-triggered responses can be finely and independently adjusted (Figure 1). Through a comprehensive physicochemical characterization, we demonstrated how controlled variations in polymer architecture translate into distinct regimes of colloidal stability, size modulation, and aggregation across pH and temperature, providing clear structure-responsivity relationships that enable the rational design of dual-responsive nanocarriers.

View Article Online  
DOI: 10.1039/D6LF00061D



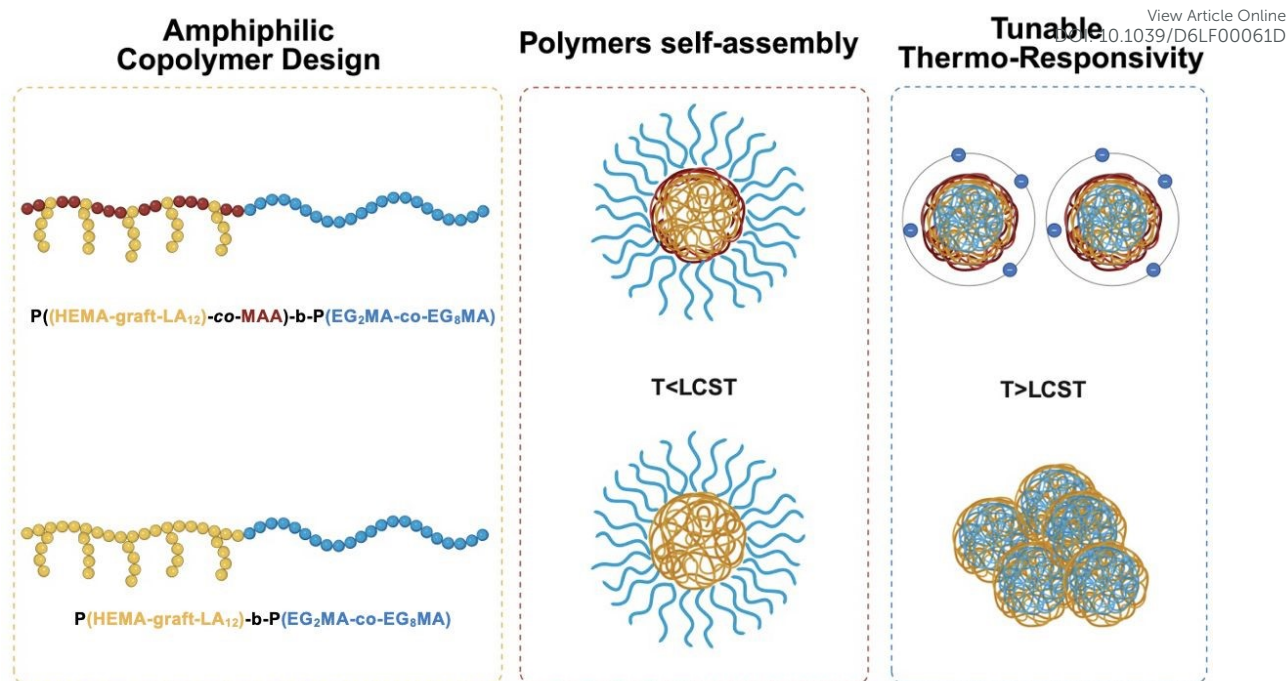


**Figure 1.** Amphiphilic block copolymer architectures incorporating a hydrophobic PLA-based core-forming segment, pH-responsive MAA units in a statistic copolymer, and a thermo-responsive PEGMA-based corona are compared with analogous PLA-PEGMA systems lacking the ionizable PMAA units. Upon dispersion in aqueous media, both polymer classes undergo spontaneous self-assembly into core-shell nanoparticles, where the relative block composition governs corona hydration, chain conformation, and interfacial stabilization. Above the LCST, nanoparticles containing PMAA preserve colloidal stability through residual electrostatic and hydration-mediated repulsive interactions, leading to controlled intraparticle corona reorganization and size contraction. In contrast, nanoparticles lacking the PMAA block undergo aggregation-driven transitions due to the absence of stabilizing interactions, resulting in the formation of supracolloidal assemblies. This architectural comparison highlights the central role of polymer composition in driving the mechanism and amplitude of thermo-responsive nanoparticle behavior.



## Experimental section

View Article Online  
DOI: 10.1039/D6LF00061D

### Materials

D, L-Lactide (Sigma Aldrich); Stannous octoate ( $\text{Sn}(\text{Oct})_2$ , Sigma Aldrich); Toluene (Sigma Aldrich); Methacrylic acid (MAA, Sigma Aldrich); 2,2'-Azobis(2-methylpropionitrile) (AIBN, Sigma Aldrich); Acetone (Sigma Aldrich); Diethyl ether (Sigma Aldrich); Dichloromethane (DCM, Sigma Aldrich); Hexane (Sigma Aldrich); Dimethyl sulfoxide (DMSO, Sigma Aldrich); Hydroxyethyl methacrylate (HEMA, Sigma Aldrich); 4-Cyano-4-[(dodecylsulfanylthiocarbonyl)sulfanyl]pentanoic acid (CTA); Dulbecco's Phosphate Buffered Saline (Sigma Aldrich); Acetonitrile (ACN; Sigma Aldrich); Tetrahydrofuran (THF; Sigma Aldrich); Ethanol (Sigma Aldrich); Di(ethylene glycol) methyl ether methacrylate (POEGMA<sub>2</sub>); Poly-(ethylene glycol) methyl ether methacrylate (POEGMA<sub>8</sub>); Phosphoric acid ( $\text{H}_3\text{PO}_4$  Sigma Aldrich); Hydrochloric acid (HCl Sigma Aldrich); Sulfuric acid ( $\text{H}_2\text{SO}_4$  Sigma Aldrich); Sodium chloride (NaCl Sigma Aldrich); triple superphosphate (TSP) were of analytical grade purity and used as received unless expressly noted.

### Synthesis of HEMA-graft-LA<sub>12</sub>

The ring-opening polymerization (ROP) of D,L-lactide was carried out using 2-hydroxyethyl methacrylate (HEMA) as the hydroxyl-terminated initiator and stannous octoate ( $\text{Sn}(\text{Oct})_2$ ) as the catalyst, in anhydrous toluene as solvent<sup>38</sup>. The targeted degree of polymerization of the polylactic acid (PLA) block was 12 lactic acid units, as defined by the initial monomer-to-initiator molar ratio. Briefly,  $\text{Sn}(\text{Oct})_2$  (0.014 g, 0.035 mmol) was first dissolved in 60 mL of toluene under continuous magnetic stirring. Once complete dissolution was achieved, D,L-lactide (6.00 g, 41.63 mmol) and HEMA (0.892 g, 6.94 mmol) were added sequentially to the reaction mixture, corresponding to a lactide-to-initiator molar ratio of 6:1. The solution was purged with nitrogen for 15 min to ensure an inert atmosphere and minimize moisture and oxygen contamination.



The reaction mixture was subsequently heated to 130 °C and maintained under constant stirring for 4 h. After completion of the polymerization, the solvent and residual volatile species were removed under reduced pressure followed by drying under high vacuum until constant weight was reached. Samples were collected at the beginning of the reaction (0 h) and at the end of the polymerization (4 h) for structural and molecular weight characterization. The conversion of D,L-lactide to PLA and the molecular weight evolution of the resulting HEMA-graft-LA<sub>12</sub> were evaluated by proton nuclear magnetic resonance (<sup>1</sup>H NMR) (Figure S1) spectroscopy and gel permeation chromatography (GPC), respectively, as described in detail in the following sections.

### Synthesis of P((HEMA-graft-LA<sub>12</sub>)-*co*-MAA)

Statistical copolymers of MAA and HEMA-graft-LA<sub>12</sub> were synthesized via reversible addition-fragmentation chain transfer (RAFT) copolymerization in hermetically sealed Pyrex vials (10 mL) placed in a thermostated heating block<sup>39</sup>. MAA and HEMA-graft-LA<sub>12</sub> in different proportions were dissolved in 5 mL of ACN under magnetic stirring. Specifically, CTA (0.028 g, 0.069 mmol) and AIBN (0.004 g, 0.023 mmol) were used at a fixed molar ratio of 1:3 (AIBN/CTA). The composition of the P((HEMA-graft-LA<sub>12</sub>)-*co*-MAA) block was tuned by simultaneously varying the relative amount of both PLA and MAA with respect to the CTA. Two target compositions were investigated, corresponding to P((HEMA-graft-LA<sub>12</sub>)<sub>12.5</sub>-*co*-MAA<sub>12.5</sub>) and P((HEMA-graft-LA<sub>12</sub>)<sub>25</sub>-*co*-MAA<sub>25</sub>), where the subscripts indicate the number of equivalents of each component relative to the moles of CTA and hence the expected degree of polymerization. In addition, a purely hydrophobic reference block consisting of P((HEMA-graft-LA<sub>12</sub>)<sub>25</sub>) without MAA was also synthesized. This compositional modulation allowed a systematic evaluation of the impact of the hydrophobic fraction on the subsequent self-assembly and thermo-responsive behavior, while maintaining identical radical and RAFT conditions across all formulations.



Once a homogeneous solution was obtained, the reaction mixture was purged with nitrogen for 30 min to remove dissolved oxygen and establish an inert atmosphere. The vials were shielded from light and heated to 70 °C, and the polymerization was allowed to proceed for 24 h under constant stirring. The conversion of HEMA-graft-LA<sub>12</sub> and MAA and the molecular weight evolution of the resulting statistical copolymers were evaluated by <sup>1</sup>H NMR spectroscopy (Figure S2) and GPC, respectively.

### **Synthesis of P((HEMA-graft-LA<sub>12</sub>)-co-MAA)-b-P(EG<sub>2</sub>MA-co-EG<sub>8</sub>MA)**

The final amphiphilic block copolymers were obtained by chain extension of the P((HEMA-graft-LA<sub>12</sub>)-co-MAA) through a second RAFT copolymerization involving the thermo-responsive monomers EG<sub>2</sub>MA and EG<sub>8</sub>MA. A library of 12 formulations was designed by systematically varying the relative feed ratio between EG<sub>2</sub>MA and EG<sub>8</sub>MA in the second block, while keeping the composition of the first P((HEMA-graft-LA<sub>12</sub>)-co-MAA) block constant within each subset of samples, in order to change only one structural degree of freedom at a time and ensure direct comparability among the different copolymer architectures. In a typical synthesis, P((HEMA-graft-LA<sub>12</sub>)-co-MAA), acting as a macromolecular CTA, together with EG<sub>2</sub>MA and EG<sub>8</sub>MA were combined in hermetically sealed pyrex vials (10 mL) and dissolved in 5 mL of ACN under magnetic stirring until a homogeneous solution was obtained. The radical initiator AIBN (0.004 g, 0.023 mmol) was then added, preserving the same molar ratio of 1:3 with respect to the CTA used in the first polymerization step. The reaction mixture was purged with nitrogen for 30 min to remove dissolved oxygen, shielded from light, and subsequently heated to 70 °C in a thermostated heating block. The polymerization was allowed to proceed for 24 h under continuous stirring. The conversion of the monomers and the molecular weight evolution of the resulting copolymers were tracked by <sup>1</sup>H NMR spectroscopy (Figure S3) and GPC (Figure S4), respectively. The feed compositions adopted for the different block copolymers are summarized in Table 1.



**Table 1.** EG<sub>2</sub>MA and EG<sub>8</sub>MA amounts for 12 different P((HEMA-graft-LA<sub>12</sub>)-co-MAA)-b-P(EG<sub>2</sub>MA-*co*-EG<sub>8</sub>MA<sub>*m*</sub>) formulations. Article Online  
DOI: 10.1039/D6LF00061D

#	Sample	EG <sub>2</sub> MA		EG <sub>8</sub> MA	
		g	mmol	g	mmol
A	P((HEMA-graft-LA <sub>12</sub> ) <sub>12.5</sub> -co-MAA <sub>12.5</sub> )-b-P(EG <sub>2</sub> MA <sub>17</sub> -co-EG <sub>8</sub> MA <sub>33</sub> )	0.216	1.15	1.150	2.30
B	P((HEMA-graft-LA <sub>12</sub> ) <sub>12.5</sub> -co-MAA <sub>12.5</sub> )-b-P(EG <sub>2</sub> MA <sub>25</sub> -co-EG <sub>8</sub> MA <sub>25</sub> )	0.325	1.73	0.865	1.73
C	P((HEMA-graft-LA <sub>12</sub> ) <sub>12.5</sub> -co-MAA <sub>12.5</sub> )-b-P(EG <sub>2</sub> MA <sub>46</sub> -co-EG <sub>8</sub> MA <sub>4</sub> )	0.597	3.17	0.140	0.28
D	P((HEMA-graft-LA <sub>12</sub> ) <sub>25</sub> -co-MAA <sub>25</sub> )-b-P(EG <sub>2</sub> MA <sub>17</sub> -co-EG <sub>8</sub> MA <sub>33</sub> )	0.216	1.15	1.150	2.30
E	P((HEMA-graft-LA <sub>12</sub> ) <sub>25</sub> -co-MAA <sub>25</sub> )-b-P(EG <sub>2</sub> MA <sub>25</sub> -co-EG <sub>8</sub> MA <sub>25</sub> )	0.325	1.73	0.865	1.73
F	P((HEMA-graft-LA <sub>12</sub> ) <sub>25</sub> -co-MAA <sub>25</sub> )-b-P(EG <sub>2</sub> MA <sub>46</sub> -co-EG <sub>8</sub> MA <sub>4</sub> )	0.597	3.17	0.140	0.28
G	P((HEMA-graft-LA <sub>12</sub> ) <sub>25</sub> -co-MAA <sub>25</sub> )-b-P(EG <sub>2</sub> MA <sub>34</sub> -co-EG <sub>8</sub> MA <sub>66</sub> )	0.432	2.30	2.300	4.60
H	P((HEMA-graft-LA <sub>12</sub> ) <sub>25</sub> -co-MAA <sub>25</sub> )-b-P(EG <sub>2</sub> MA <sub>50</sub> -co-EG <sub>8</sub> MA <sub>50</sub> )	0.65	3.46	1.730	3.46
I	P((HEMA-graft-LA <sub>12</sub> ) <sub>25</sub> -co-MAA <sub>25</sub> )-b-P(EG <sub>2</sub> MA <sub>92</sub> -co-EG <sub>8</sub> MA <sub>8</sub> )	1.194	6.34	0.280	0.56
J	P(HEMA-graft-LA <sub>12</sub> ) <sub>25</sub> -b-P(EG <sub>2</sub> MA <sub>17</sub> -co-EG <sub>8</sub> MA <sub>33</sub> )	0.216	1.15	1.150	2.30
K	P(HEMA-graft-LA <sub>12</sub> ) <sub>25</sub> -b-P(EG <sub>2</sub> MA <sub>25</sub> -co-EG <sub>8</sub> MA <sub>25</sub> )	0.325	1.73	0.865	1.73
L	P(HEMA-graft-LA <sub>12</sub> ) <sub>25</sub> -b-P(EG <sub>2</sub> MA <sub>46</sub> -co-EG <sub>8</sub> MA <sub>4</sub> )	0.216	1.15	1.150	2.30

### Nanoparticle Production

Polymeric nanoparticles were prepared by solvent displacement of the amphiphilic block copolymers in aqueous medium<sup>40</sup>. Briefly, 50 mg of polymer were first dissolved in 1 mL of ACN to obtain a clear and homogeneous solution. The organic phase was then added dropwise into 10 mL of distilled water contained in a 25 mL glass vial and magnetically stirred at 600 rpm, using a 200  $\mu$ L calibrated micropipette to ensure a controlled addition rate.



Upon contact with water, spontaneous nanoparticle formation occurred because of polymer self-assembly driven by solvent exchange. The resulting colloidal suspension was maintained under stirring for at least 30 min to allow complete equilibration and stabilization of the nanoparticle population. After nanoparticle formation, the colloidal suspension was transferred into a dialysis membrane with a molecular weight cut-off of 3.5 kDa and dialyzed against distilled water for 3 h to remove residual ACN prior to DLS characterization. The size and morphology of the produced nanoparticles were further investigated by TEM using an EFTEM Leo 912AB microscope operating at 80 kV (Carl Zeiss, Jena, Germany). Samples were prepared by placing a 5  $\mu$ L drop of nanoparticle dispersion onto a Formvar/carbon-coated copper grid. The samples were allowed to dry overnight before imaging. Three conditions were analyzed for a representative formulation: nanoparticles dried at room temperature, nanoparticles dried at 45  $^{\circ}$ C after and nanoparticles acidified to pH 3 prior to deposition and drying. Digital images were acquired using a CCD camera (Esi Vision Proscan camera).

### Physicochemical characterization of polymers and nanoparticles

The molecular weight and dispersity of the synthesized polymers and their intermediate precursors were determined by GPC using a Jasco LC-2000 Plus chromatographic system equipped with a refractive index detector (RI-2031 Plus, Jasco). Separation was achieved using three Agilent PLgel columns ( $5 \times 10^{-6}$  m particle size,  $300 \times 7.5$  mm, molecular weight separation range  $5 \times 10^2$ - $1.7 \times 10^6$  g mol $^{-1}$ ). Samples were prepared by dissolving the polymers in tetrahydrofuran (THF) at a concentration of 4 mg mL $^{-1}$ , followed by filtration through a 0.2  $\mu$ m PTFE membrane prior to injection. Polystyrene standards from 580 to 3'250'000 g mol $^{-1}$  were employed for calibration, and blank runs were performed using pure THF. The hydrodynamic size, surface charge, and stimulus-dependent colloidal behavior of the nanoparticles were investigated by DLS using a Zetasizer Nano ZS (Malvern Instruments) operating at a scattering angle of 173 $^{\circ}$ .



For each measurement, 100  $\mu\text{L}$  of nanoparticle suspension were diluted in 2.9 mL of distilled water or buffer solutions covering a pH range from 1 to 14 with unit increments. An aliquot of 1 mL of the resulting dispersion was transferred into glass cuvettes for analysis. The refractive index was set to 1.590 and the absorption coefficient to 0.010. Temperature-dependent measurements were carried out by equilibrating the samples at the desired temperature prior to data acquisition. Optical transmittance experiments were performed to probe the pH-responsiveness of the nanoparticle dispersions using a Jasco V-630 UV-vis spectrophotometer. For pH-dependent studies, nanoparticle suspensions were diluted in buffer solutions at different pH using the same dilution protocol described above, and 1 mL of each sample was transferred into high-performance quartz cuvettes. Temperature-triggered measurements were instead carried out in distilled water. Changes in optical transmittance were monitored as a function of the external stimulus to capture variations in colloidal stability and aggregation state. The critical micelle concentration (CMC) of the polymeric systems was determined by fluorescence spectroscopy using pyrene as a polarity-sensitive probe on a Jasco FP-8500 spectrofluorometer. A defined amount of pyrene, initially dissolved in acetone, was deposited into clean glass vials, and the solvent was allowed to completely evaporate. Polymer solutions with concentrations ranging from 5000 to 0.001  $\text{mg L}^{-1}$  were subsequently added to each vial, yielding a final pyrene concentration of  $6 \times 10^{-7}$  M. The samples were incubated in the dark at room temperature for 24 h to reach equilibrium. Fluorescence emission spectra were collected in the 350-450 nm range upon excitation at 335 nm, using slit widths of 5 nm (excitation) and 2 nm (emission). The intensity ratio between the third ( $I_3$ , 384 nm) and the first ( $I_1$ , 373 nm) vibronic bands of pyrene ( $I_3/I_1$ ) was used to determine the onset of micellization.

View Article Online  
DOI: 10.1039/D6LF00061D



## Statistical analysis

View Article Online  
DOI: 10.1039/D6LF00061D

Where applicable, experimental data were analyzed using ANOVA analysis of variance. Statistical significance was set to p value  $< 0.05$ . Results are presented as mean value  $\pm$  standard deviation.



## Results and discussion

### Design and molecular characterization of the polymer library

The synthetic strategy adopted in this work relied on a three-step hierarchical approach to generate well-defined amphiphilic block copolymers with independently tunable hydrophobic, pH-responsive and thermo-responsive segments (Figure 2).

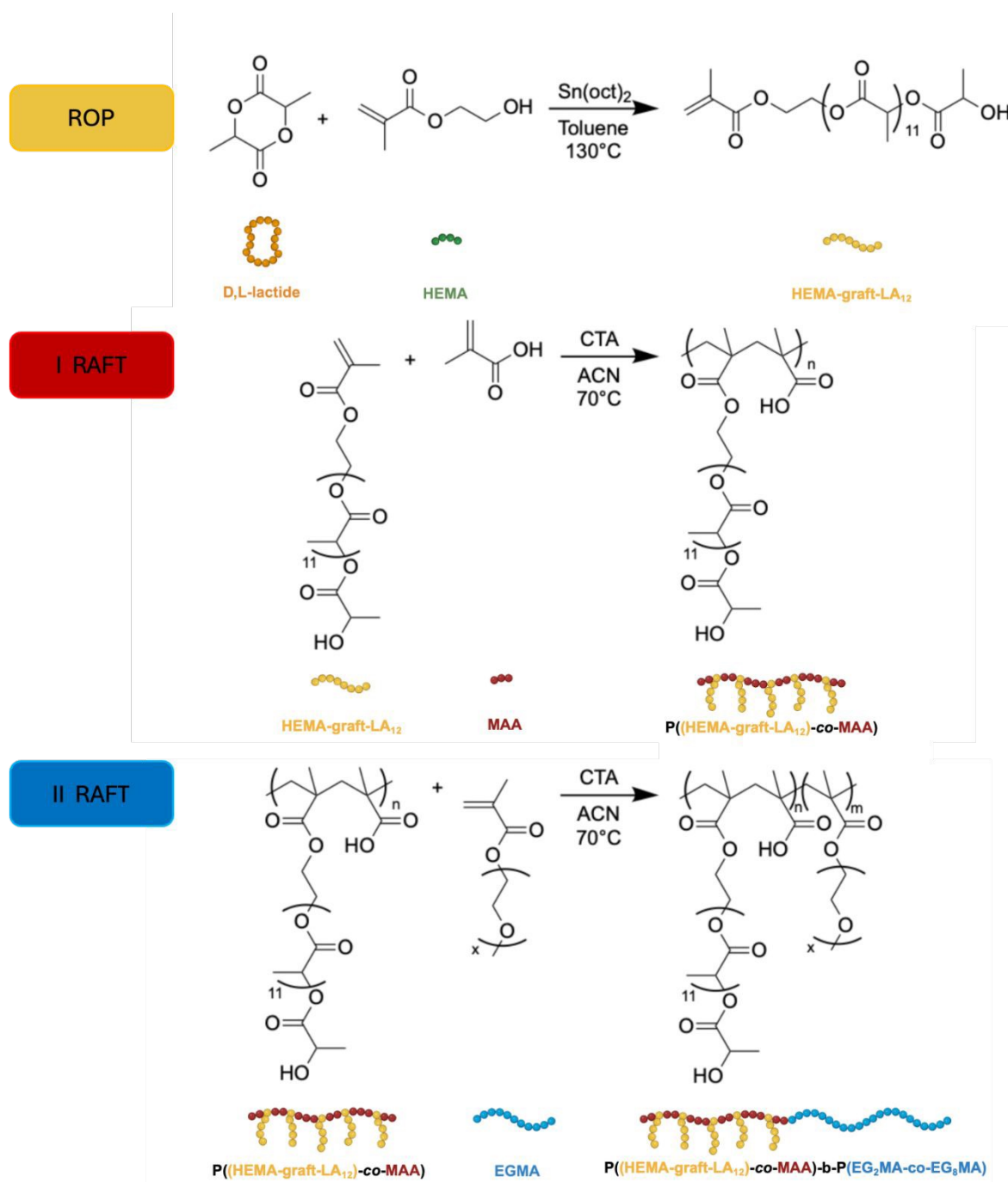
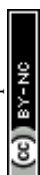


**Figure 2.** Sequential polymerization strategy for the synthesis of amphiphilic block copolymers via ROP and RAFT polymerization.



In a first step, D,L-lactide was polymerized by ROP using HEMA as initiator, yielding a vinyl-terminated PLA macromonomer suitable for subsequent RAFT polymerization. This intermediate provided a precisely controlled hydrophobic scaffold while preserving a polymerizable methacrylate handle for further chain growth. The successful formation of the HEMA-graft-LA<sub>12</sub> precursor was confirmed by <sup>1</sup>H NMR spectroscopy (Figure S1), showing the appearance of characteristic PLA resonances together with the vinyl protons of the terminal methacrylate group, confirming the retention of end-group functionality after ROP. GPC (Figure S4) and <sup>1</sup>H NMR analysis indicated the formation of low molecular weight PLA oligomers with narrow molecular weight distribution, consistent with the targeted short hydrophobic chain (Table 2). The detailed equations used for <sup>1</sup>H NMR-based conversion analysis and molecular weight estimation, including the definition of the integrated resonances used for each synthetic step, are reported in the Supporting Information. The experimental number-average molecular weight was in good agreement with the theoretical value calculated from the monomer-to-initiator feed ratio, corresponding to an average PLA length of approximately 12 lactic acid repeating units, thereby confirming effective control over the ROP process. In the second step, the HEMA-graft-LA<sub>12</sub> was employed in a first RAFT copolymerization with MAA to generate the amphiphilic precursor block P((HEMA-graft-LA<sub>12</sub>)-co-MAA). Two targeted degrees of polymerization were investigated, namely P((HEMA-graft-LA<sub>12</sub>)<sub>12.5</sub>-co-MAA<sub>12.5</sub>) and P((HEMA-graft-LA<sub>12</sub>)<sub>25</sub>-co-MAA<sub>25</sub>), together with a purely hydrophobic P(HEMA-graft-LA<sub>12</sub>)<sub>25</sub> reference in which the MAA comonomer was avoided. The controlled growth of this statistical copolymer was first assessed by kinetic analysis. High monomer conversion could be achieved for both HEMA-graft-LA<sub>12</sub> and MAA (Figure 3a), with the corresponding natural logarithm of the ratio between initial and instantaneous monomer concentration (ln(M<sub>0</sub>/M)) growing linearly with time (Figure 3b), indicating a constant radical concentration and a limited contribution of termination reactions, as expected for a well-controlled RAFT process.



Consistently,  $^1\text{H}$  NMR (Figure S2) and GPC analysis (Figure S3) showed a progressive increase in number-average molecular weight with increasing targeted chain length, while maintaining relatively low dispersity values ( $D \leq 1.41$ ) across all formulations (Table 2). The experimental molecular weights followed the expected theoretical trend derived from monomer conversion and feed composition. In the final step, the P((HEMA-graft- $\text{LA}_{12}$ )-co-MAA) macro-CTAs were chain-extended via a second RAFT polymerization with thermo-responsive  $\text{EG}_2\text{MA}$  and  $\text{EG}_8\text{MA}$ , affording a library of 12 different block copolymers with systematically varied shell and corona composition (Samples A-L).  $^1\text{H}$  NMR spectroscopy enabled the quantitative evaluation of block composition and molecular weight from the relative integration of the characteristic resonances. This trend was fully consistent with the kinetic analysis of the second RAFT step, where high monomer conversion could be achieved (Figure 3c) with linear  $\ln(M_0/M)$  during time (Figure 3d), confirming the preservation of controlled radical propagation during chain extension. All final copolymers exhibited narrow molecular weight distributions ( $D$  ranging from 1.06 to 1.24), indicating that the living character of the RAFT process was retained even in the presence of bulky and highly solvated oligo(ethylene glycol) side chains <sup>41</sup>.

View Article Online  
DOI: 10.1039/D6LF00061D



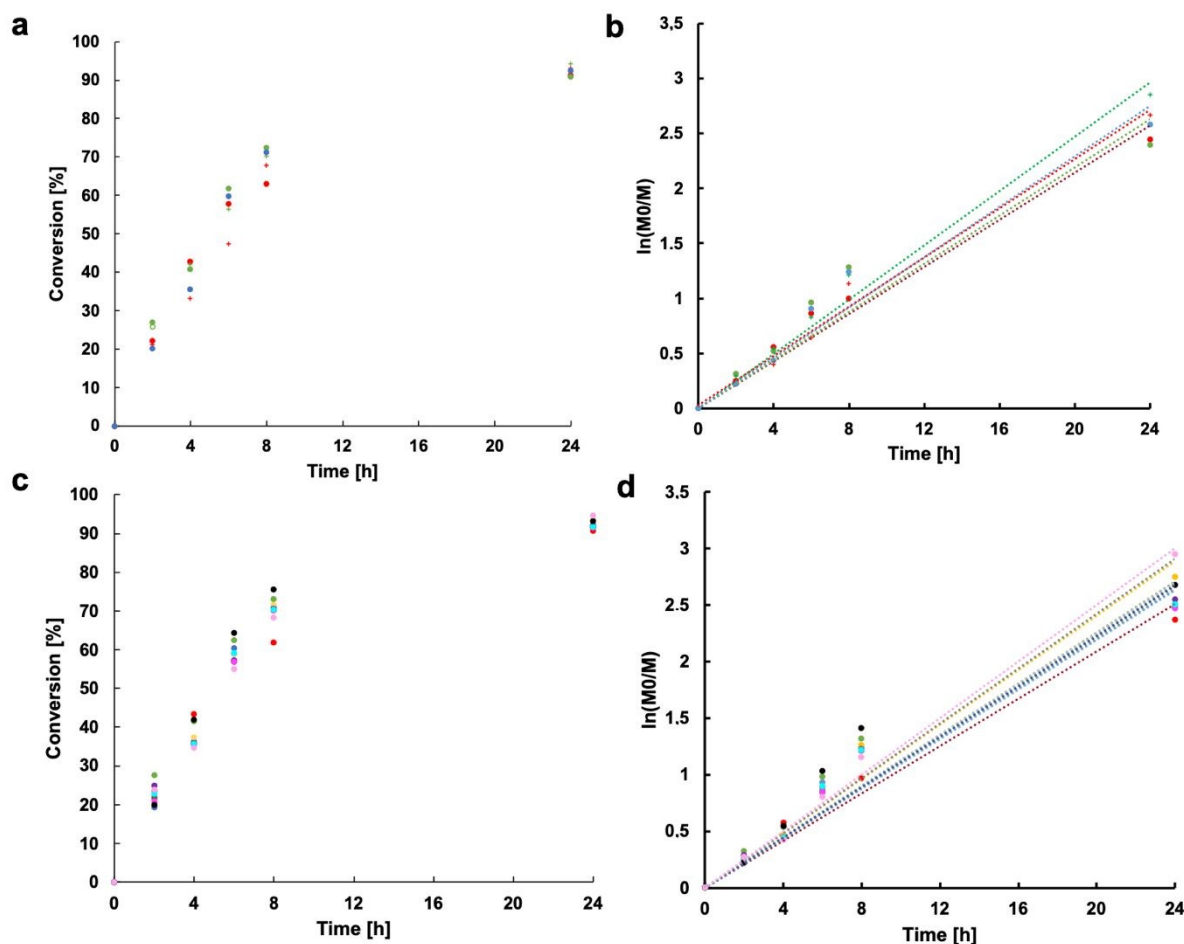


**Figure 3.** (a, b) Monomer conversion and corresponding semilogarithmic plots of the ratio between initial ( $M_0$ ) and instantaneous ( $M$ ) monomer concentration as a function of time for the RAFT polymerization of the P((HEMA-graft- $LA_{12}$ ) $_{12.5}$ -co- $MAA_{12.5}$ ) (red), P((HEMA-graft- $LA_{12}$ ) $_{25}$ -co- $MAA_{25}$ ) (green), and P(HEMA-graft- $LA_{12}$ ) $_{25}$  (blue). Circular symbols represent the corresponding property referred to HEMA-graft- $LA_{12}$ , while cross symbols correspond to MAA. (c, d) Monomer conversion and semilogarithmic plots of the ratio between initial ( $M_0$ ) and instantaneous ( $M$ ) monomer concentration as a function of time for the RAFT polymerization of the thermo-responsive EGnMA block during the chain-extension step. Colors correspond to the different formulations as follows: Sample A (red), B (green), C (blue), D (yellow), E (grey), F (brown), G (orange), H (purple), I (magenta), J (cyan), K (black) and L (pink). The name of the samples refer to the architecture reported in Table 2.



Across the entire library, the experimentally determined molecular weights were in reasonable agreement with the theoretical values calculated from the targeted degrees of polymerization and monomer feed ratios (Table 2). Minor deviations observed for selected formulations, particularly at higher EG<sub>8</sub>MA content, can be attributed to differences in monomer reactivity and to the intrinsic limitations of GPC calibration using polystyrene standards for amphiphilic and highly solvated polymers. Nevertheless, the overall consistency of the molecular parameters demonstrates that the multistep synthetic route enables reliable and modular control over block length, composition, and dispersity, providing a solid molecular basis for the subsequent investigation of self-assembly and stimulus-responsive behavior.

View Article Online  
DOI: 10.1039/D6LF00061D



**Table 2.** Average molecular weights obtained by GPC and  $^1\text{H}$  NMR for the HEMA-graft- $\text{LA}_{12}$  macromonomer, P(HEMA-graft- $\text{LA}_{12}$ )-CO-MAA) macro-CTAs, and final block copolymers. Monomer conversion values ( $\chi$ ) and experimental degrees of polymerization (DP) determined by  $^1\text{H}$  NMR are also reported. For the first RAFT copolymerization step, the conversions of HEMA-graft- $\text{LA}_{12}$  and MAA are reported separately and listed on consecutive rows. The subscripts in the sample names refer to the targeted feed degrees of polymerization, while the reported DP values correspond to the experimentally estimated values. Detailed equations and calculation procedures for  $M_n$ , conversion, and DP determination are provided in the Supporting Information.

#	Sample	<i>T</i>				$^1\text{H}$ NMR					
		$M_n$ (Da)	$M_n$ (Da)	$M_w$ (Da)	$\bar{D}$ (-)	$M_n$ (Da)	$\chi$ (%)	DP $\text{LA}_{12}$	DP MAA	DP $\text{EG}_2\text{MA}$	DP $\text{EG}_8\text{MA}$
-	HEMA-graft- $\text{LA}_{12}$	890	893	1553	1.74	913	-	12.31	-	-	-
-	P((HEMA-graft- $\text{LA}_{12}$ ) $_{12.5}$ -co-MAA $_{12.5}$ )	12576	12430	16284	1.31	11793	91.3	11.41	11.64	-	-
-	P((HEMA-graft- $\text{LA}_{12}$ ) $_{25}$ -co-MAA $_{25}$ )	25152	27463	35152	1.28	23144	90.9	22.72	23.57	-	-
-	P(HEMA-graft- $\text{LA}_{12}$ ) $_{25}$	23000	25289	35657	1.41	21480	92.5	23.12	-	-	-
A	P((HEMA-graft- $\text{LA}_{12}$ ) $_{12.5}$ -co-MAA $_{12.5}$ )-b-P( $\text{EG}_2\text{MA}_{17}$ -co- $\text{EG}_8\text{MA}_{33}$ )	31786	33940	36774	1.08	33222	90.6	11.41	11.64	18.49	35.90
B	P((HEMA-graft- $\text{LA}_{12}$ ) $_{12.5}$ -co-MAA $_{12.5}$ )-b-P( $\text{EG}_2\text{MA}_{25}$ -co- $\text{EG}_8\text{MA}_{25}$ )	29672	31415	36724	1.17	29488	91.6	11.41	11.64	25.71	25.71
C	P((HEMA-graft- $\text{LA}_{12}$ ) $_{12.5}$ -co-MAA $_{12.5}$ )-b-P( $\text{EG}_2\text{MA}_{46}$ -co- $\text{EG}_8\text{MA}_4$ )	24121	23814	26475	1.11	24123	91.8	11.41	11.64	53.22	4.63
D	P((HEMA-graft- $\text{LA}_{12}$ ) $_{25}$ -co-MAA $_{25}$ )-b-P( $\text{EG}_2\text{MA}_{17}$ -co- $\text{EG}_8\text{MA}_{33}$ )	46339	46726	53776	1.15	50459	93.6	22.72	23.57	23.57	45.76
E	P((HEMA-graft- $\text{LA}_{12}$ ) $_{25}$ -co-MAA $_{25}$ )-b-P( $\text{EG}_2\text{MA}_{25}$ -co- $\text{EG}_8\text{MA}_{25}$ )	44224	36770	45041	1.22	50246	91.8	22.72	23.57	28.31	28.31
F	P((HEMA-graft- $\text{LA}_{12}$ ) $_{25}$ -co-MAA $_{25}$ )-b-P( $\text{EG}_2\text{MA}_{46}$ -co- $\text{EG}_8\text{MA}_4$ )	38674	42730	50489	1.18	48395	91.6	22.72	23.57	68.21	5.93
G	P((HEMA-graft- $\text{LA}_{12}$ ) $_{25}$ -co-MAA $_{25}$ )-b-P( $\text{EG}_2\text{MA}_{34}$ -co- $\text{EG}_8\text{MA}_{66}$ )	64473	60450	69862	1.16	68723	91.8	22.72	23.57	39.33	76.35
H	P((HEMA-graft- $\text{LA}_{12}$ ) $_{25}$ -co-MAA $_{25}$ )-b-P( $\text{EG}_2\text{MA}_{50}$ -co- $\text{EG}_8\text{MA}_{50}$ )	60244	57803	63090	1.09	62467	92.1	22.72	23.57	57.14	57.14
I	P((HEMA-graft- $\text{LA}_{12}$ ) $_{25}$ -co-MAA $_{25}$ )-b-P( $\text{EG}_2\text{MA}_{92}$ -co- $\text{EG}_8\text{MA}_8$ )	49142	29371	36317	1.24	56434	91.5	22.72	23.57	132.6	11.5
J	P(HEMA-graft- $\text{LA}_{12}$ ) $_{25}$ -b-P( $\text{EG}_2\text{MA}_{17}$ -co- $\text{EG}_8\text{MA}_{33}$ )	42035	46331	55719	1.20	51544	91.8	23.12	-	25.94	50.36
K	P(HEMA-graft- $\text{LA}_{12}$ ) $_{25}$ -b-P( $\text{EG}_2\text{MA}_{25}$ -co- $\text{EG}_8\text{MA}_{25}$ )	39920	50494	53423	1.06	48854	93.1	23.12	-	39.78	39.78
L	P(HEMA-graft- $\text{LA}_{12}$ ) $_{25}$ -b-P( $\text{EG}_2\text{MA}_{46}$ -co- $\text{EG}_8\text{MA}_4$ )	34370	37742	42161	1.12	39192	94.8	23.12	-	76.44	6.65



## Nanoparticle Self-Assembly and Colloidal Stability across the Polymer Library

View Article Online  
DOI: 10.1039/D6LF00061D

The physicochemical properties of the nanoparticles obtained from the polymer library are summarized in Table 3, including hydrodynamic diameter, polydispersity index, surface charge, phase separation temperature (PST), diameter change upon heating, critical micelle concentration, and phase separation pH. These parameters provide a comprehensive overview of the structural and colloidal characteristics of each formulation and establish the basis for correlating polymer architecture with nanoparticle stability and stimulus-responsive behavior.

**Table 3.** Physicochemical properties of the nanoparticles produced from the self-assembly of the 12 amphiphilic block copolymers. PST values were operationally assigned only when the hydrodynamic diameter variation reached or exceeded 20% with respect to the initial low-temperature value.  $\Delta D$  was calculated as the difference between the hydrodynamic diameter measured in the high-temperature plateau region and that measured in the low-temperature plateau region.

Sample	<i>D</i> (nm)	PDI (-)	Z-pot (mV)	PST (°C)	$\Delta D$ (nm)	CMC	pH-resp
A	214	0.132	-23	-	-17.28	2.86	6
B	119	0.078	-25	-	-14.71	3.14	6
C	81.6	0.149	-21	-	-13.48	2.41	6
D	210	0.091	-53	42	-24.76	8.46	4
E	131	0.156	-47	34	-36.42	3.92	4
F	78	0.104	-49	32	-27.38	4.33	4
G	244	0.073	-33	38	-59.01	15.82	5
H	182	0.139	-29	32	-55.66	11.70	5
I	93	0.086	-30	30	-50.26	10.49	5
J	102	0.121	-5	38	276.30	1.70	-
K	82	0.157	-7	36	563.40	1.80	-
L	80	0.095	-4	34	766.10	1.55	-

Nanoparticle self-assembly is governed by the amphiphilic molecular architecture of the copolymers. The covalent connection between the PLA-grafted methacrylate units, the ionizable MAA units, and the EGMA-based thermo-responsive block imposes a fixed spatial organization that promotes core-shell nanoparticle formation upon solvent displacement.

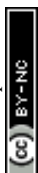


In water, the hydrophobic PLA side chains minimize contact with the aqueous phase and drive core formation through hydrophobic association<sup>42</sup>. Conversely, MAA units and EGMA side chains remain preferentially exposed to water, providing electrostatic, hydration-mediated, and steric stabilization. At neutral pH, deprotonated MAA groups generate electrostatic repulsion between particles, while hydrated EGMA chains contribute to corona solvation. Upon heating, dehydration of the EGMA block promotes corona collapse, whereas residual MAA ionization counterbalances interparticle aggregation<sup>43</sup>. Under acidic conditions, protonation of MAA reduces electrostatic stabilization and enhances interchain association, leading to aggregation<sup>44</sup>. All synthesized block copolymers spontaneously self-assembled into colloiddally stable nanoparticles upon solvent displacement in aqueous media. The initial hydrodynamic diameter and PDI measured at room temperature are summarized in Table 3 for the entire polymer library (samples A-L). Across all formulations, nanoparticle production was highly reproducible, yielding well-defined colloidal dispersions with diameters spanning from approximately 80 to 240 nm and PDI values typically below 0.16, indicative of narrow size distributions and good colloidal uniformity. A clear dependence of nanoparticle size on the molecular architecture was observed across the polymer library. The twelve formulations were intentionally organized in subsets of three, in which the composition of the first block was kept constant while the thermo-responsive block was systematically varied following the same incremental trend in EG<sub>2</sub>MA/EG<sub>8</sub>MA ratio. This experimental design enabled a direct comparison of the effect of corona composition and length on nanoparticle size under otherwise identical core conditions. Within each subset, increasing the EG<sub>2</sub>MA/EG<sub>8</sub>MA ratio resulted in a progressive decrease in hydrodynamic diameter. For copolymers bearing the shorter amphiphilic precursor P((HEMA-graft-LA<sub>12</sub>)<sub>12.5</sub>-co-MAA<sub>12.5</sub>) (samples A-C), particle size decreased from 214 nm (sample A) to 82 nm (sample C) as the fraction of EG<sub>2</sub>MA increased.

View Article Online  
DOI: 10.1039/D6LF00061D



This behavior reflects the progressive replacement of EG<sub>8</sub>MA units, characterized by longer and more hydrated side chains, with the more compact EG<sub>2</sub>MA monomers, leading to a reduction of the hydration volume of the corona and a lower contribution of the shell to the hydrodynamic radius. A fully consistent evolution was observed for the P((HEMA-graft-LA<sub>12</sub>)<sub>25</sub>-co-MAA<sub>25</sub>) series (samples D-F), where particle size decreased from 210 nm (sample D) to 78 nm (sample F) following the same increase in EG<sub>2</sub>MA content, confirming that the structural role of the thermo-responsive block dominates the nanoparticle size independently of the absolute core length. An additional level of control emerges when formulations, sharing identical EG<sub>2</sub>MA/EG<sub>8</sub>MA ratio, are compared across increasing absolute block length (samples A-D-G, B-E-H, and C-F-I). Under these conditions, a systematic enlargement of nanoparticle size is observed upon increasing the degree of polymerization of the thermo-responsive block, indicating that the absolute chain length directly modulates corona hydration and steric extension, thereby increasing its contribution to the overall hydrodynamic radius. In parallel, the influence of the first block became evident when comparing amphiphilic and purely hydrophobic core architectures. The smallest particle size was consistently observed for the samples lacking the ionizable MAA units (samples J-L), which exhibit a more compact core packing driven by purely hydrophobic interactions. The impact of block composition on self-assembly was further reflected in the CMC. The CMC of the copolymers was determined using pyrene as a hydrophobic fluorescent probe. At low polymer concentrations, the ratio between the intensities of the third to first emission band  $I_3/I_1$  was in the range 0.55-0.57 indicating that pyrene remained predominantly dispersed in the aqueous phase, confirming the absence of organized hydrophobic domains. Upon increasing polymer concentration, a gradual increase in the  $I_3/I_1$  ratio was observed, reflecting the progressive formation of hydrophobic microenvironments associated with micelle nucleation (Figure 4).



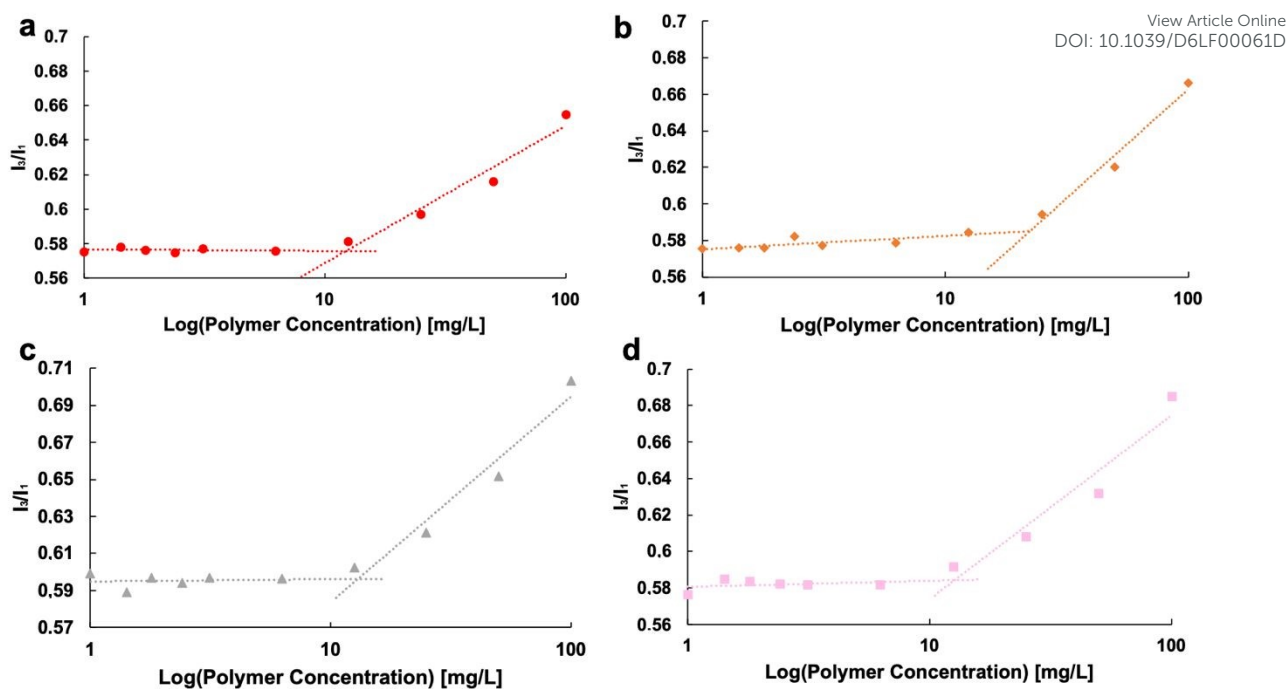
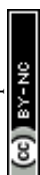


**Figure 4.** Determination of the CMC of representative nanoparticle formulations using pyrene as hydrophobic fluorescent probe. The ratio between the third and first vibronic emission peaks ( $I_3 = 384$  nm/ $I_1 = 373$  nm) is plotted as a function of the logarithm of polymer concentration. Each panel corresponds to a different structural family within the polymer library: (a) sample A (red circles), (b) sample I (orange diamonds), (c) sample E (gray triangles), and (d) sample L (pink squares).

The CMC was defined as the inflection point of the  $I_3/I_1$  versus concentration plots and was found to span a broad range across the polymer library (1.55-15.82 mg/L), consistent with the wide modulation of hydrophobic-hydrophilic balance introduced by the different block architectures. Amphiphilic copolymers containing the MAA block displayed systematically higher CMC values compared to the PLA-only analogues (samples J-L), consistent with the additional hydrophilic contribution of the MAA units and their enhanced solvation in aqueous media. In contrast, copolymers lacking MAA exhibited the lowest CMC values (1.55-1.80 mg L<sup>-1</sup>), highlighting the stronger hydrophobic driving force for aggregation in the absence of ionizable groups.



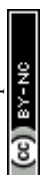
Within the amphiphilic series, increasing EG<sub>8</sub>MA content was generally associated with higher CMC values, reflecting the progressively larger hydration volume and steric extension of the thermo-responsive corona, which reduces the tendency toward micellization. This trend is fully consistent with the size analysis, where EG<sub>8</sub>MA-rich formulations generated more swollen assemblies due to the dominant contribution of the hydrated shell. TEM analysis was performed on sample E as a representative formulation to provide complementary morphological evidence of the stimulus-responsive behavior (Figure S9). Under physiological pH conditions, the nanoparticles appeared well dispersed, with an average diameter of approximately 130 nm, in agreement with the DLS data. After drying at 45 °C, the NPs remained individually distinguishable but displayed a reduced average diameter, slightly below 100 nm, consistent with temperature-induced nanoparticle shrinking. In contrast, samples exposed to acidic conditions at pH 3 showed the formation of large aggregated structures, in which individual nanoparticles could no longer be clearly distinguished, supporting the occurrence of pH-triggered colloidal destabilization.

### pH-Responsive Behavior

The pH-responsive behavior of the nanoparticle library was found to strongly depend on the effective surface charge density, as quantified by zeta potential measurements. As expected, samples J-L realized without MAA were characterized by near-neutral zeta potentials (-4 to -7 mV), and did not exhibit any detectable phase separation pH (PSPH), confirming that ionizable groups are required to enable electrostatically driven structural transitions. For amphiphilic systems containing MAA units, a clear correlation emerged between the magnitude of the negative zeta potential and the pH at which phase separation was observed, in terms of a sharp increase in the nanoparticle size. Copolymers with lower MAA content (samples A-C) displayed moderately negative zeta potentials (approximately -21 to -25 mV) and exhibited pH-responsiveness around pH 6.



In these systems, the reduced density of ionizable groups leads to an earlier neutralization of surface charge upon acidification, facilitating interchain association under mildly acidic conditions. In contrast, copolymers with higher MAA content (samples D-F) exhibited significantly more negative zeta potentials (-47 to -53 mV) and a pronounced shift of the pH-responsiveness toward more acidic values ( $\text{pH} \approx 4$ ), as stronger protonation is required to effectively screen electrostatic repulsion. Samples featuring the same MAA content but a longer and more hydrated thermo-responsive corona (samples G-I) displayed intermediate zeta potentials (-29 to -33 mV) and pH-responsiveness centred around pH 5. This behavior indicates that increased corona hydration and steric shielding partially screen the effective surface charge, shifting the destabilization threshold toward intermediate pH values despite identical nominal MAA content. Overall, the library can therefore be classified into four distinct electrostatic regimes: non-ionizable systems with no pH-responsiveness, low-charge systems responding at mildly acidic pH, high-charge systems requiring stronger acidification, and screened-charge systems exhibiting intermediate behavior. This stratification highlights that pH-responsiveness is governed not only by the absolute amount of MAA incorporated in the polymer chain, but by the effective charge exposure and its modulation by chain architecture and corona hydration. To ensure that these regimes reflect intrinsic structural behavior rather than formulation-specific variability, the pH-dependent trends were consistently evaluated using three independent observables, namely zeta potential, hydrodynamic size by DLS, and optical transmittance. For clarity, the reported pH profiles correspond to four averaged trends, each representative of one structural family obtained by averaging three formulations sharing identical core composition and MAA content but differing in thermo-responsive shell architecture. This approach reinforces the robustness of the identified regimes and emphasizes the underlying structure-property relationships.



Upon decreasing pH, the progressive reduction of negative surface charge was accompanied by a marked increase in particle size and turbidity for the MAA-containing formulations (Figure 5), indicating the onset of interparticle association and partial loss of colloidal stabilization. Conversely, at higher pH values, strongly negative zeta potentials correlated with stable hydrodynamic diameters and high optical transmittance, reflecting well-dispersed nanoparticle populations. The convergence of these independent techniques confirms that the identified pH-responsivity windows reflect genuine colloidal and structural rearrangements rather than artefacts associated with a single measurement modality.

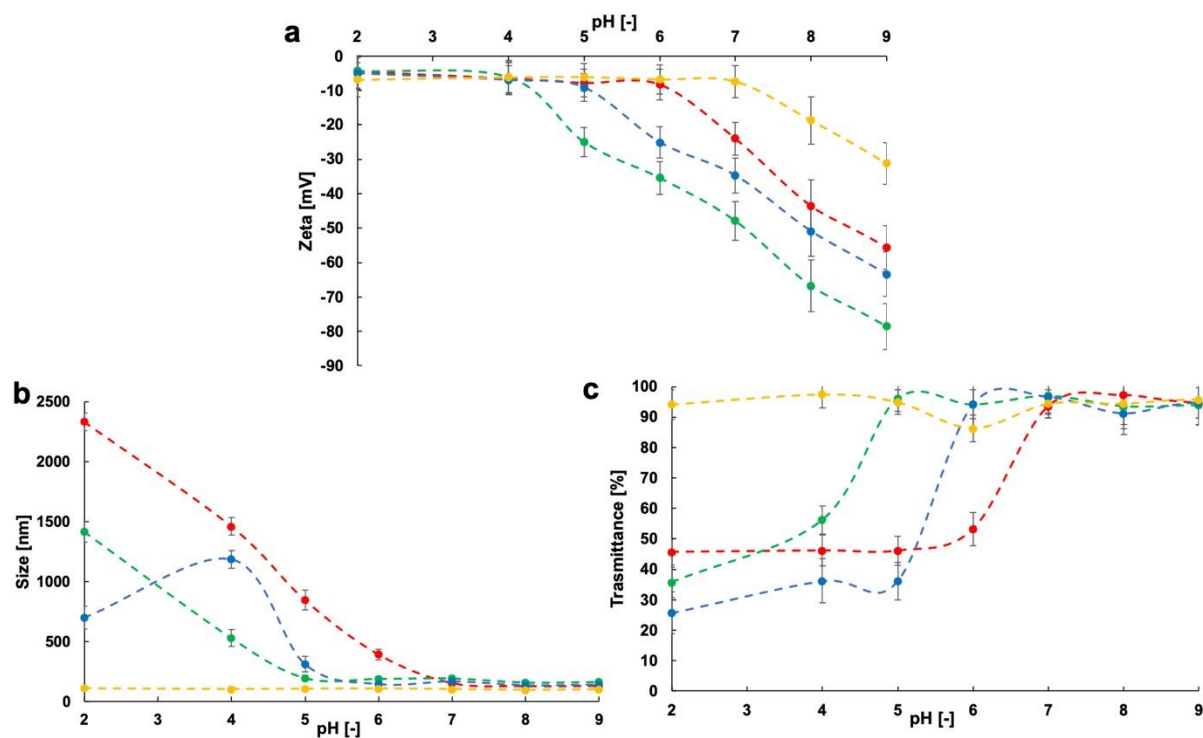


**Figure 5.** pH-dependent electrostatic and colloidal response of the nanoparticle library grouped into structural families. (a) Zeta potential, (b) hydrodynamic diameter (DLS), and (c) optical transmittance at 500 nm (UV-vis) as a function of pH. Curves correspond to averaged datasets obtained from four formulations sharing identical core composition and MAA content but different thermo-responsive shell architectures. Red: samples A-C; green: samples D-F; blue: samples G-I; yellow: samples J-L.



## Thermo-Responsive Behavior

View Article Online  
DOI: 10.1039/D6LF00061D

The thermo-responsive behavior of the nanoparticle library was evaluated by monitoring the evolution of hydrodynamic diameter as a function of temperature by DLS (Figure 6). The amplitude of the transition was quantified as  $\Delta D$ , defined as the difference between the hydrodynamic diameter measured in the plateau region above the phase separation temperature and that measured in the plateau region below the transition.

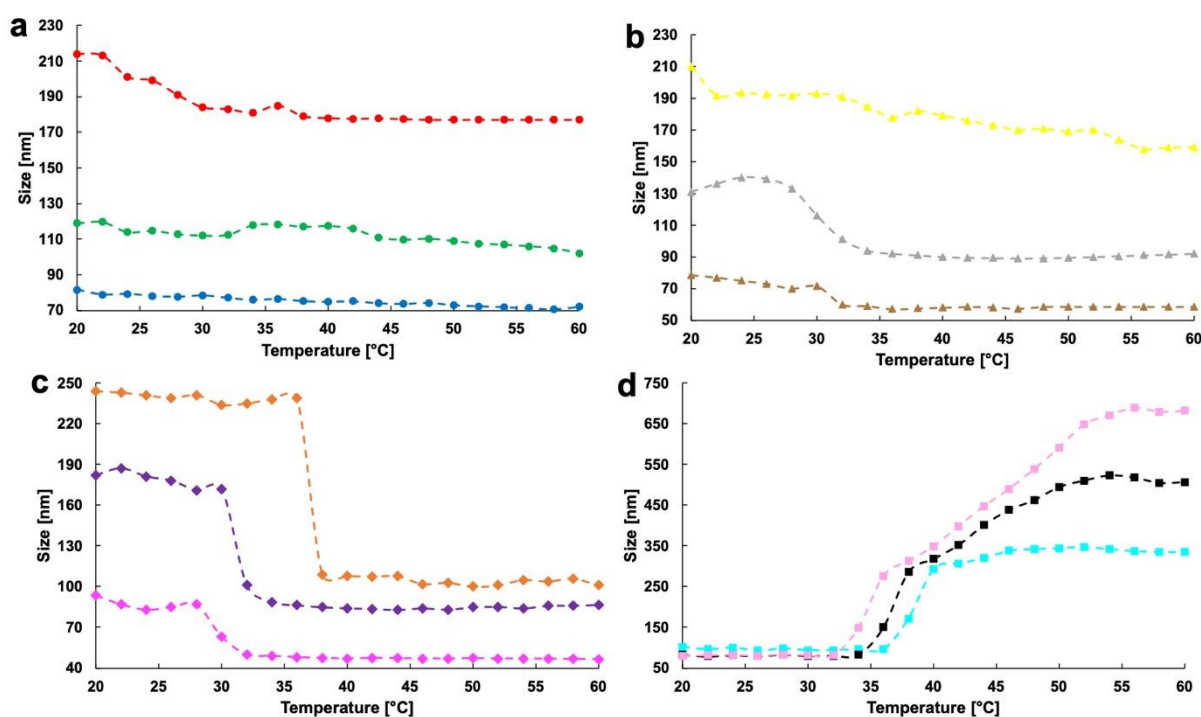
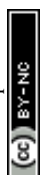
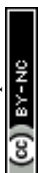


**Figure 6.** Hydrodynamic diameter of nanoparticle formulations A-L as a function of temperature measured by DLS. Color code: A (red), B (green), C (blue), D (yellow), E (grey), F (brown), G (orange), H (purple), I (magenta), J (cyan), K (black), and L (pink).

A clear separation emerges when nanoparticles containing the P((HEMA-graft-LA<sub>12</sub>)-co-MAA) block (Samples A-I) are compared with those lacking MAA (samples J-L). The former displayed smooth sigmoidal size-temperature profiles, characterized by moderate and reproducible diameter variations across the transition and by well-defined plateaus above the separation temperature.



In addition, temperature-dependent optical transmittance UV-vis measurements were performed for samples J–L to complement the DLS analysis of thermo-responsive behavior (Figure S10). These samples were selected because they lack MAA stabilizing units and display aggregation-dominated transitions upon heating, as evidenced by the large increase in hydrodynamic diameter measured by DLS. Under these conditions, interparticle aggregation is expected to increase turbidity and decrease optical transmittance, making UV-vis analysis particularly informative. In contrast, MAA-containing formulations primarily undergo intraparticle shrinking while preserving colloidal stability, and therefore do not exhibit a strong turbidity response. Samples J-L showed a marked decrease in transmittance above the PST, confirming the onset of aggregation-driven turbidity upon heating. In these systems, the temperature-triggered response is dominated by the progressive dehydration and compaction of the oligo(ethylene glycol)-based corona, while the presence of the hydrophilic and ionizable MAA-containing block provides electrostatic stabilization. As a result, the transition corresponds to a structural reorganization process, in which individual nanoparticles reversibly adjust their hydrodynamic diameter without losing colloidal identity. In contrast, the counterparts with no MAA exhibited a fundamentally different response. Although their transition temperatures fall within a similar thermal window, the size-temperature profiles display a sharp and abrupt increase in diameter upon crossing the transition temperature, followed by the formation of a plateau at large particle size. The associated  $\Delta D$  values are one order of magnitude larger than those observed for PLA-MAA-containing systems, indicating a transition dominated by interparticle aggregation rather than by intraparticle conformational rearrangement. The absence of the MAA units eliminates both electrostatic stabilization and hydrophilic shielding at the particle interface, so that the collapse of the thermo-responsive chains directly promotes extensive interparticle association and the formation of supracolloidal assemblies. Within the PLA-MAA series, both the transition temperature and the amplitude of the size response could be independently tuned through polymer architecture.



The phase separation temperatures span a practically relevant range of approximately 30–44 °C with this parameter increasing with the content in EG<sub>8</sub>MA in the corona, as already reported previously<sup>25,45,46</sup>. On the other hand,  $\Delta D$  varies systematically with the length and hydration capacity of the thermo-responsive corona. Formulations featuring longer and more hydrated shells display larger absolute contractions, consistent with a greater contribution of corona dehydration to the overall hydrodynamic radius. This trend is particularly evident for the extended-corona architectures (Samples G-I), which exhibit the largest  $\Delta D$  values within the PLA-MAA-containing family, whereas shorter-corona systems show more limited size modulation. Not only the total length of the corona-forming block, but also its composition influenced the observed  $\Delta D$ . In particular, the larger the mole fraction of EG<sub>8</sub>MA in the thermo-responsive portion, the larger the shrinking of the nanoparticles (more negative  $\Delta D$ ). This is consistent with the already mentioned major contribution of EG<sub>8</sub>MA in driving the overall size of the colloids, which upon reorganization leads to the stronger contraction of the corona. On the other side, for samples dominated by interparticle interactions (samples J-L), the positive increase in  $\Delta D$  becomes less and less accentuated as the mole fraction of EG<sub>8</sub>MA increases. This suggests that these more hydrophilic units preserve a certain hydration even above the phase separation temperature, mitigating the aggregation. Despite these substantial differences in  $\Delta D$ , PLA-MAA-containing nanoparticles preserve well-defined plateaus both below and above the transition, indicating stable colloidal states on both sides of the LCST. This decoupling between transition temperature and response amplitude enables fine control over nanoparticle size as a function of temperature while maintaining colloidal integrity, in contrast to the aggregation-driven switching observed for PLA-only systems. From a design standpoint, the polymer library therefore enables access to two distinct thermo-responsive regimes: a high-amplitude aggregation regime driven by interparticle association, and a controlled size modulation regime governed by reversible corona dehydration.



The ability to selectively access and quantitatively tune these regimes through rational block design provides a robust platform for engineering thermo-triggered nanostructures with quantitatively programmable structural responses.

View Article Online  
DOI: 10.1039/D6LF00061D

### 3.5. Structural Correlation and Definition of a Growth Number (GN)

To rationalize the distinct thermo-responsive regimes observed across the polymer library, a growth number (GN) was introduced as a phenomenological structural descriptor linking polymer architecture to the amplitude and nature of the size evolution across the LCST. The GN is defined as:

$$GN = \frac{DP_{EGMA} * DP_{MAA} + DP_{EG8MA}}{DP_{TOT}} \quad (1)$$

$DP_{EGMA}$  corresponds to the degree of polymerization of the thermo-responsive oligo(ethylene glycol)-based block obtained by summing up the number of repeating units of  $EG_2MA$  and  $EG_8MA$ ,  $DP_{MAA}$  accounts for the ionizable methacrylic acid units, and  $DP_{TOT}$  is the total degree of polymerization of the copolymer. Each term reflects a distinct physical contribution. The thermo-responsive block provides the driving force for the transition, as dehydration of the oligo(ethylene glycol) side chains above the PST generates an entropically favoured collapse of the corona. Increasing  $DP_{EGMA}$  amplifies the magnitude of this collapse and the associated change in polymer-water interactions. The MAA block plays a stabilizing role by providing residual charge and persistent hydration above the LCST. As long as  $DP_{MAA} > 0$ , electrostatic barriers prevent direct interparticle contact, confining the thermo-induced collapse to an intraparticle reorganization of the corona. In contrast, the hydrophobic PLA units promote aggregation above the LCST by enhancing interparticle attraction once the thermo-responsive chains collapse. In the present formulation, this contribution is structurally encoded in the normalization term  $DP_{TOT}$ , which includes the hydrophobic PLA segment.



Increasing  $DP_{PLA}$  therefore enlarges the total degree of polymerization and reduces the relative magnitude of GN, shifting the system toward an aggregation-dominated regime. The additional additive contribution  $DP_{EG8MA}$  accounts for the distinct structural role of the longer oligo(ethylene glycol) side chains, which enhance hydration volume and steric shielding within the corona. This term introduces an architecture-dependent modulation that differentiates EG<sub>8</sub>-rich coronas from EG<sub>2</sub>-dominated ones, explaining the systematic divergence observed within each structural subgroup. The chosen normalized multiplicative-additive formulation of the GN captures the cooperative balance between dehydration-driven corona collapse, electrostatic stabilization, and hydrophobic attraction within a single structural descriptor (Figure 7).

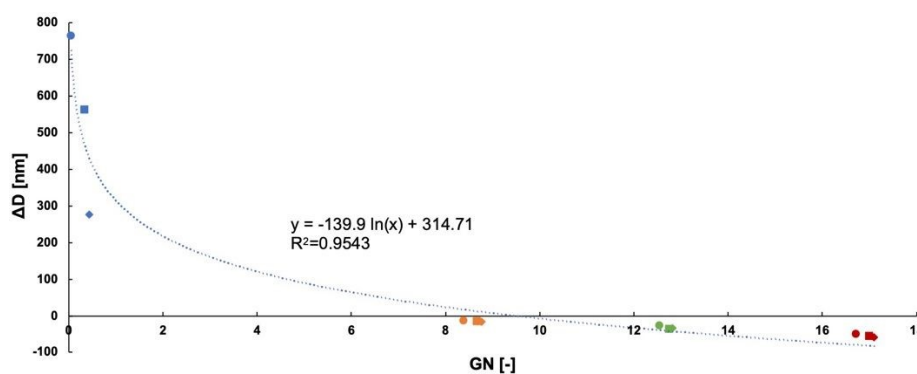


**Figure 7.** Circles denote samples A, D, G, and J; squares denote samples B, E, H, and K; diamonds denote samples C, F, I, and L. Colors identify the structural families as follows: orange (A-C), green (D-F), red (G-I), and blue (J-L).

High GN values correspond to systems in which a strong corona collapse is effectively counterbalanced by electrostatic stabilization, resulting in controlled, negative  $\Delta D$  values associated with reversible intraparticle shrinkage. Conversely, when GN approaches zero, the stabilizing contribution of MAA vanishes and the same dehydration-driven collapse leads to extensive aggregation and a large, positive increase in apparent hydrodynamic diameter.



Importantly, GN is not intended as a rigorous thermodynamic parameter, but as a structural index that condenses the competing roles of corona collapse, hydrophobic aggregation, and electrostatic stabilization into a single descriptor. The monotonic correlation observed between GN and  $\Delta D$  confirms that the thermo-responsive behavior of the nanoparticles is governed by the relative balance of these architectural elements rather than by any individual block alone.

## Conclusions

This work establishes a structurally programmable platform for dual pH- and thermo-responsive polymeric nanoparticles, in which molecular architecture directly encodes the nature, amplitude, and direction of the thermo-induced structural transition. By systematically tuning the relative contributions of the hydrophobic core, ionizable stabilizing units, and thermo-responsive corona, we demonstrated that the nanoparticle behavior can be precisely controlled across two fundamentally distinct regimes: aggregation-dominated transitions leading to supracolloidal assembly, and controlled intraparticle corona collapse resulting in reversible nanoparticle shrinking while preserving colloidal identity. The introduction of GN provides a simple yet powerful structural descriptor capable of predicting this transition, revealing that nanoparticle fate is governed by the balance between corona dehydration, electrostatic stabilization, and hydrophobic attraction rather than by any single block alone. This finding establishes a direct structure/responsivity relationship and transforms dual-responsive nanoparticles from empirically optimized systems into structurally programmable nanomaterials. From a translational perspective, the ability to engineer nanoparticles that undergo controlled shrinking or aggregation in response to physiologically relevant temperature and pH variations opens new opportunities for localized drug delivery. Shrinking nanoparticles may enhance tissue penetration and intracellular uptake, while aggregation-prone systems may promote local retention and depot formation.



The modular nature of this platform further enables independent tuning of responsiveness, size and stability, providing a versatile framework for designing adaptive nanocarriers tailored to specific biological microenvironments.

## SUPPORTING INFORMATION

<sup>1</sup>H NMR spectra of the synthesized copolymers during RAFT polymerization; GPC chromatograms of the synthesized copolymers; critical micelle concentration determination.

## CONFLICTS OF INTEREST

There are no conflicts to declare.

## DATA AVAILABILITY

All data presented in this manuscript can be provided by the corresponding author on reasonable demand.

## REFERENCES

- 1 A. Balcerak-Woźniak, M. Dzwonkowska-Zarzycka and J. Kabatc-Borcz, *Materials*, 2024, **17**, 4255.
- 2 G. Nunziata, F. Pizzetti, P. Veglianesi, G. Forloni, C. Balducci and F. Rossi, *Expert Opinion on Drug Delivery*.
- 3 M. Sponchioni, U. Capasso Palmiero and D. Moscatelli, *Materials Science and Engineering: C*, 2019, **102**, 589.
- 4 A. K. Philip, B. A. Samuel, Y. S. Saleh, B. I. Mohammad and H. A. Al-Aubaidy, *Drug Development and Industrial Pharmacy*, 2025, **0**, 1–16.
- 5 G. Nunziata, D. Pollonio, E. Lacroce and F. Rossi, *Materials Today Chemistry*, 2025, **49**, 103063.
- 6 H. S. El-Sawy, A. M. Al-Abd, T. A. Ahmed, K. M. El-Say and V. P. Torchilin, *ACS nano*, 2018, **12**, 10636–10664.
- 7 H. Sabit, T. M. Pawlik, F. Radwan, M. Abdel-Hakeem, S. Abdel-Ghany, A.-H. S. Wadan, M. Elzawahri, A. El-Hashash and B. Arneht, *Molecular Cancer*, 2025, **24**, 160.
- 8 N. Mamidi, F. F. De Silva and A. O. Mahmoudsalehi, *Nanoscale*, 2025, **17**, 7673–7696.
- 9 L. Eltaib, *Polymers*, 2025, **17**, 833.
- 10 M. R. Dreher, W. Liu, C. R. Michelich, M. W. Dewhirst and A. Chilkoti, *Cancer research*, 2007, **67**, 4418–4424.
- 11 D. R. Heintzman, E. L. Fisher and J. C. Rathmell, *Cellular & molecular immunology*, 2022, **19**, 316–326.



- 12B. T. Mai, S. Fernandes, P. B. Balakrishnan and T. Pellegrino, *Accounts of chemical research*, 2018, **51**, 999–1013. View Article Online  
DOI: 10.1039/D6LF00061D
- 13G. Nunziata, M. Nava, E. Lacroce, F. Pizzetti and F. Rossi, *Macromolecular Rapid Communications*, 2025, 2401127.
- 14T. Blondy, J. Poly, C. Linot, J. Boucard, E. Allard-Vannier, S. Nedellec, P. Hulin, C. Hénoumont, L. Larbanoix, R. N. Muller, S. Laurent, E. Ishow and C. Blanquart, *Nanoscale*, 2022, **14**, 5884–5898.
- 15K. Ishimoto, M. Arimoto, T. Okuda, S. Yamaguchi, Y. Aso, H. Ohara, S. Kobayashi, M. Ishii, K. Morita, H. Yamashita and N. Yabuuchi, *Biomacromolecules*, 2012, **13**, 3757–3768.
- 16Y. Stetsyshyn, H. Ohar, A. Budkowski and G. Lazzara, *Polymers*, 2025, **17**, 1580.
- 17R. Ortega-Córdova, K. Sánchez-Carillo, S. Carrasco-Saavedra, G. Ramírez-García, M. G. Pérez-García, J. F. A. Soltero-Martínez and J. D. Mota-Morales, *RSC Appl. Interfaces*, 2024, **1**, 600–611.
- 18T. Ougizawa and T. Inoue, *Polymer journal*, 1986, **18**, 521–527.
- 19V. V. Yashin, F. Mahmood, K. Saravanamuttu and A. C. Balazs, *RSC Appl. Interfaces*, 2024, **1**, 183–193.
- 20G. Conzatti, S. Cavalie, C. Combes, J. Torrisani, N. Carrère and A. Tourrette, *Colloids and Surfaces B: Biointerfaces*, 2017, **151**, 143–155.
- 21R. Konefał, J. Spěvák, G. Mužíková and R. Laga, *European Polymer Journal*, 2020, **124**, 109488.
- 22G. Nunziata, F. Pizzetti, V. Veneruso, A. Rossetti, E. Petillo, E. Frigerio, C. Marabelli, M. Tiboni, L. Casertari, P. Veglianesi, A. Sacchetti and F. Rossi, *Materials Today Chemistry*, 2026, **53**, 103587.
- 23G. Nunziata, E. Limiti, D. Aramini, M. Nava, L. Moretti, A. Rainer, M. Sponchioni and F. Rossi, *ACS Applied Materials & Interfaces*.
- 24A. Christopoulou, C. Kazamiakis, Z. Iatridi and G. Bokias, *Polymers*, 2024, **16**, 1456.
- 25M. Sponchioni, R. Ferrari, L. Morosi and D. Moscatelli, *Journal of Polymer Science Part A: Polymer Chemistry*, 2016, **54**, 2919–2931.
- 26M. Rey, J. Kolker, J. A. Richards, I. Malhotra, T. S. Glen, N. D. Li, F. H. Laidlaw, D. Renggli, J. Vermant and A. B. Schofield, *Nature communications*, 2023, **14**, 6723.
- 27S. Bochenek, F. Camerin, E. Zaccarelli, A. Maestro, M. M. Schmidt, W. Richtering and A. Scotti, *Nature Communications*, 2022, **13**, 3744.
- 28N. Manfredini, M. Tomasoni, M. Sponchioni and D. Moscatelli, *Polymers*, DOI:10.3390/polym13071032.
- 29B. Baptista, A. S. R. Oliveira, P. Mendonça, A. C. Serra, J. F. J. Coelho and F. Sousa, *Biomaterials Advances*, 2023, **145**, 213267.
- 30M. Zhang, X. Peng, Y. Ding, X. Ke, K. Ren, Q. Xin, M. Qin, J. Xie and J. Li, *Materials horizons*, 2023, **10**, 2554–2567.
- 31E. Lacroce, G. Nunziata, F. Cianniello, E. Limiti, A. Rainer, F. B. Vangosa, A. Sacchetti, M. Sponchioni and F. Rossi, *International Journal of Biological Macromolecules*, 2024, 137659.
- 32H. Farmanbordar, M. S. Amini-Fazl and R. Mohammadi, *Journal of Drug Delivery Science and Technology*, 2021, **66**, 102896.
- 33V. Ghalekhondabi, A. Fazlali and M. Soleymani, *Journal of Molecular Liquids*, 2022, **348**, 118028.
- 34Y. Zheng, L. Wang, L. Lu, Q. Wang and B. C. Benicewicz, *ACS Omega*, 2017, **2**, 3399–3405.
- 35B. M. Asghari, M. S. Zadeh, H. A. Panahi, S. H. Tackallou and R. Safaeijavan, *Journal of Molecular Liquids*, 2023, **390**, 123155.



- 36 F. Adeli, F. Abbasi, M. Babazadeh and S. Davaran, *Journal of nanobiotechnology*, 2022, **20**, 91. View Article Online  
DOI: 10.1039/D6LF00061D
- 37 M. Schifone, G. Nunziata and F. Rossi, *Advances in Colloid and Interface Science*, 2026, **355**, 103913.
- 38 M. J.-L. Tschan, R. M. Gauvin and C. M. Thomas, *Chem. Soc. Rev.*, 2021, **50**, 13587–13608.
- 39 G. Moad, *Polym. Chem.*, 2017, **8**, 177.
- 40 L. Han, Y. Yu, P. Li and Y. Tian, *RSC Appl. Interfaces*, 2026, **3**, 26–44.
- 41 M.-N. Antonopoulou, R. Whitfield, N. P. Truong and A. Anastasaki, *European Polymer Journal*, 2022, **174**, 111326.
- 42 Y. Yu, R. Ferrari, M. Lattuada, G. Storti, M. Morbidelli and D. Moscatelli, *Journal of Polymer Science Part A: Polymer Chemistry*, 2012, **50**, 5191–5200.
- 43 Á. M. López, A. Tirado-Guizar, A. Licea-Claverie and A. Ramírez-Jiménez, *Macromolecular Research*, 2022, **30**, 917–929.
- 44 A. Balafouti and S. Pispas, *Pharmaceutics*, 2023, **15**, 1198.
- 45 J. F. Lutz, *J. Polym. Sci. A Polym. Chem.*, 2008, **46**, 3459.
- 46 J.-F. Lutz, A. Hoth and K. Schade, *Designed monomers and polymers*, 2009, **12**, 343–353.



**Data availability**

View Article Online  
DOI: 10.1039/D6LF00061D

All data presented in this manuscript can be provided by the corresponding author on reasonable demand.

